







Article

Zinc Oxide/Phosphorus-Doped Carbon Nitride Composite as Potential Scaffold for Electrochemical Detection of Nitrofurantoin

Faheem Ahmed ^{1,*}, Thangavelu Kokulnathan ^{2,*}, Ahmad Umar ^{3,4,*}, Sheikh Akbar ⁴, Shalendra Kumar ^{1,5}, Nagih M. Shaalan ^{1,6}, Nishat Arshi ⁷, Mohd Gulfam Alam ⁸, Abdullah Aljaafari ¹ and Adil Alshoaibi ¹

¹ Department of Physics, College of Science, King Faisal University, P.O. Box 400, Al-Ahsa 31982, Saudi Arabia

² Department of Electro-Optical Engineering, National Taipei University of Technology, Taipei 106, Taiwan

³ Department of Chemistry, Faculty of Science and Arts and Promising Centre for Sensors and Electronic Devices (PCSED), Najran University, Najran 11001, Saudi Arabia

⁴ Department of Materials Science and Engineering, The Ohio State University, Columbus, OH 43210, USA

⁵ Department of Physics, School of Engineering, University of Petroleum & Energy Studies, Dehradun 248007, India

⁶ Physics Department, Faculty of Science, Assiut University, Assiut 71516, Egypt

⁷ Department of Basic Sciences, Preparatory Year Deanship, King Faisal University, P.O. Box 400, Al-Ahsa 31982, Saudi Arabia

⁸ Department of Chemistry, Faculty of Science, Islamic University of Madinah, Madinah 42351, Saudi Arabia

* Correspondence: fahmed@kfu.edu.sa (F.A.); kokul49@gmail.com (T.K.); ahmadumar786@gmail.com (A.U.)

Abstract: Herein, we present an electrocatalyst constructed by zinc oxide hexagonal prisms/phosphorus-doped carbon nitride wrinkles (ZnO HPs/P-CN) prepared via a facile sonochemical method towards the detection of nitrofurantoin (NF). The ZnO HPs/P-CN-sensing platform showed amplified response and low-peak potential compared with other electrodes. The exceptional electrochemical performance could be credited to ideal architecture, rapid electron/charge transfer, good conductivity, and abundant active sites in the ZnO HPs/P-CN composite. Resulting from these merits, the ZnO HPs/P-CN-modified electrode delivered rapid response (2 s), a low detection limit (2 nM), good linear range (0.01–111 μM), high sensitivity (4.62 $\mu\text{A } \mu\text{M}^{-1} \text{cm}^2$), better selectivity, decent stability ($\pm 97.6\%$), and reproducibility towards electrochemical detection of NF. We further demonstrated the feasibility of the proposed ZnO HPs/P-CN sensor for detecting NF in samples of water and human urine. All the above features make our proposed ZnO HPs/P-CN sensor a most promising probe for detecting NF in natural samples.

Keywords: metal oxide; carbonous material; heteroatom; antibiotic medication



Citation: Ahmed, F.; Kokulnathan, T.; Umar, A.; Akbar, S.; Kumar, S.; Shaalan, N.M.; Arshi, N.; Alam, M.G.; Aljaafari, A.; Alshoaibi, A. Zinc Oxide/Phosphorus-Doped Carbon Nitride Composite as Potential Scaffold for Electrochemical Detection of Nitrofurantoin.

Biosensors **2022**, *12*, 856. <https://doi.org/10.3390/bios12100856>

Received: 12 September 2022

Accepted: 6 October 2022

Published: 10 October 2022

Publisher's Note: MDPI stays neutral with regard to jurisdictional claims in published maps and institutional affiliations.



Copyright: © 2022 by the authors. Licensee MDPI, Basel, Switzerland. This article is an open access article distributed under the terms and conditions of the Creative Commons Attribution (CC BY) license (<https://creativecommons.org/licenses/by/4.0/>).

1. Introduction

Water is an indispensable and precious reserve for every living entity to sustain life in this world [1–3]. With human activities and the industrial revolution, water sources have become contaminated with various types of pollutants, which bring serious harm to human beings and other organisms throughout the world [3]. The chief water contaminants are households, organic materials, drug manufacturers, large-scale animal feeding operations, organic materials, industries, and pharmaceutical residues [4–6]. Notably, the World Health Organization revealed that nearly 30% of individuals living rurally need hygienic water sources, and more than 2,000,000 humans die every year from contamination of drinkable water [7–9]. Among the different pollutants, the most notorious are pharmaceutical residues, which harm biodiversity. Every day, approximately 35 billion defined daily-dose pharmaceutical items are devoured around the world [9]. After their use, the improper disposal of unused, unwanted, and expired pharmaceutical compounds into the biosphere is the cause of pollution as well as other negative impacts [10,11]. Among the several types

of pharmaceutical products, antibiotics have gained special attention due to their ability to develop antimicrobial resistance strains, their extensive usage, low degradation properties, and even causing death, if serious [12,13].

Antibiotics are medicines broadly used to treat or prevent bacterial infections in microorganisms as well as growth promoters in animal husbandry and aquaculture, which have been identified as significant pollutants in water [14,15]. Nitrofurantoin (NF) is one of the most commonly used nitrofuran antibiotics for the treatment of skin sensitizer, amebicide, fungicide, coccidiosis infections, bladder cancer, anti-inflammatory, and infections in the urinary tract [16–24]. Over use and the residues of NF produce a series of side effects such as pulmonary toxicity, neuropathy, flatulence, drowsiness, dizziness, numbness, hepatotoxicity, and other reactions. Even worse, the metabolic path of nitro-containing groups (NF) is reduced into the cytotoxic products (reactive oxygen species and NO• radicals) [25,26]. Hence, NF is often released into the environment foremost as an ecological system contagion, which can be hazardous even at a low-level amount [21–25]. On behalf of these reasons, many countries (United States, European Union, Australia, Brazil, China, Thailand, and the Philippines) have strictly prohibited the usage of NF due to its severe effects against all living organisms and the ecosystem. Roughly 1% of NF is eliminated as aminofurantoin in urine from original form [16].

Likewise, from the drug (expired pills) and trade production waste (residues) of NF that is directly discharged into local groundwaters, rivers, and soils, it may cause severe well-being effects in both human beings and other living microbes. Therefore, it is essential to stringently supervise the residual levels of NF in potable water and biological samples. The conventional methods such as colorimetry, photoluminescence, polarography, flow injection-spectrophotometry, surface-enhanced Raman spectroscopy, high-performance liquid chromatography, and flow injection-spectrophotometry were used for detecting NF [16–18,21–30]. Amongst the mentioned analytical methods, one of the most ideal platforms for the detection of trace amounts of molecules in food and environmental samples is the electrochemical sensor, due to their special features including high sensitivity, low cost, excellent selectivity, and portability [31–34]. However, the traditional electrode is usually limited by sluggish kinetics with low electrochemical performance and high overpotentials. Electrochemical sensor performances are dependent on electrocatalysts that play a vital role to produce amplified peak intensity and low-on-set peak potential.

In this sense, metal oxides (MOs) in the electrochemical sensors' field have been considered promising electrocatalysts [35]. Amongst a wealth of MOs, zinc oxide (ZnO) has gained extensive attention as an electrode material for electrochemical sensors owing to its conspicuous advantages such as biocompatibility, tunable bandgap, non-toxicity, economic synthesis, and good catalytic activity [36–39]. Up to now, various types of morphology have been reported for ZnO such as spheres, pompons, mushrooms, rods, wires, cubes, aggregates, wrinkles, hexagonal prisms, plates, and so on [36,40–43]. In particular, the hexagonal prism's structure may be a preferable candidate for electrochemical detection. Substantial research pursuits were devoted to improving the stability and conductivity, including ZnO incorporation into desirable conductive materials that could enhance the electrocatalytic activity. According to previous knowledge, the two-dimensional graphitic-carbon nitride (g-CN) with a unique property is regarded as a potential catalyst for electrochemical sensing [43–45].

Recently, non-metal heteroatom-doped g-CN has ignited tremendous research interests in electrochemical sensors owing to it modifying the physicochemical properties such as active sites, electronic conductivity, synergy, more defects, charge transfer mobility, high stability, its electronic structure, and excellent biocompatibility [46,47]. Phosphorus-doped g-CN could greatly modulate the physicochemical properties [48–52]. Based on the above statements, P-CN was chosen to be the supporting material for the electrochemical sensing. To date, no work was carried out on electrochemical sensing using P-CN-modified electrodes. Herein, a ZnO HPs/P-CN composite was designed and synthesized via a facile sonochemical method, and further utilized modified electrode material for NF sensing.

The fabricated electrode presented excellent electrochemical activity to NF compared with the other electrodes. Moreover, the proposed electrochemical platform was productively applied to detect NF in biological and water samples with high accuracy.

2. Experimental Details

2.1. Chemicals and Reagents

Zinc acetate tetrahydrate ($\text{Zn}(\text{CH}_3\text{CO}_2) \geq 98\%$), hexamethylenetetramine (HMTA, $(\text{CH}_2)_6\text{N}_4 \geq 99\%$), ammonium fluoride ($\text{NH}_4\text{F} \geq 98\%$), nitrofurantoin (NF), N, N-dimethylformamide, and melamine were purchased from Sigma Aldrich and Merck and used without further purification. All the electrochemical experiments were carried out using 0.05 M phosphate buffer (PB) as the supporting electrolyte.

2.2. Synthesis of P-CN

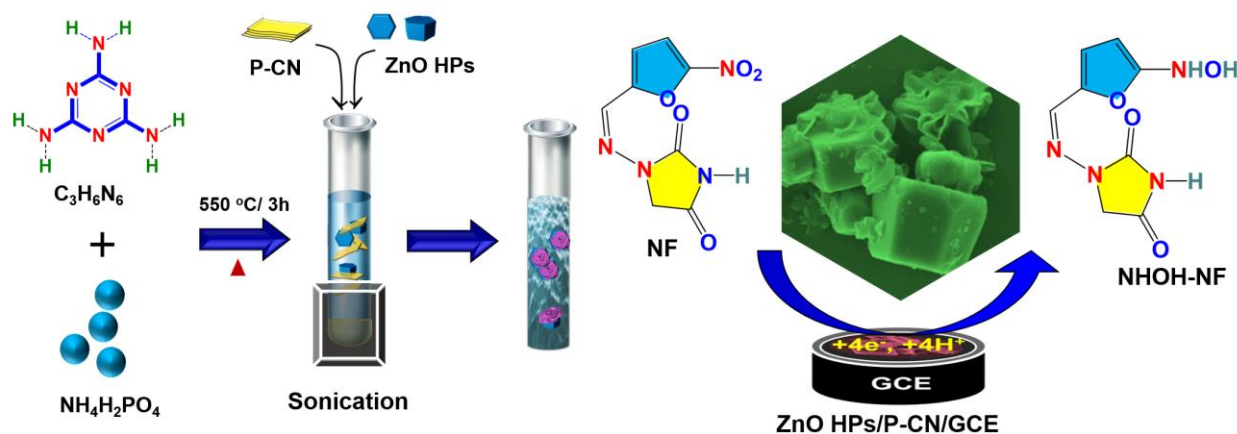
The wrinkled P-CN were prepared by thermal polymerization method [53]. Briefly, a definite quantity of $\text{C}_3\text{H}_6\text{N}_6$ was dispersed into 50 mL DI water under vigorous stirring. With vigorous stirring, an appropriate amount of $\text{NH}_4\text{H}_2\text{PO}_4$ was added to the aforesaid solution and kept for 1 h to prepare the homogenous mixture. The product was then collected by centrifugation and dried at 50°C in the oven. Then, the product was transferred into the muffle furnace under an air atmosphere to heat for about 3 h at 550°C . Finally, the P-CN was washed by DI water multiple times to get rid of unreacted impurities and was dried overnight. For comparison, g-CN was prepared without $\text{NH}_4\text{H}_2\text{PO}_4$ in a similar process.

2.3. Synthesis of ZnO HPs

The ZnO HPs were prepared using the hydrothermal method [54,55]. In the classic synthesis, 0.1 M of $\text{Zn}(\text{CH}_3\text{CO}_2)_2$ was dissolved in 40 mL of DI water and stirred for 15 min. After that, 3 mmol of HMTA and 6 mmol of NH_4F were slowly injected into the above solution under vigorous stirring and the mixture was stirred for 1 h. Next, the mixture was placed in a stainless-steel autoclave to carry out the hydrothermal reaction at 180°C for about 12 h in an air oven. The precipitate was then collected by centrifugation, washed many times in ethanol and DI water, and dried overnight. Finally, the as-prepared ZnO HPs were calcined for a period of 3 h at 400°C under air-atmosphere.

2.4. Synthesis of ZnO HPs/P-CN Composite

The ZnO HPs/P-CN composite was synthesized via a facile sonochemical technique as schematically illustrated in Scheme 1. Briefly, ZnO HPs and P-CN were taken in 1:1 ratio and ultrasonicated for 3 h, followed by overnight drying at 50°C to form a ZnO/P-CN composite.



Scheme 1. Schematic to prepare ZnO HPs/P-CN composite for electrochemical detection of NF.

2.5. Instrumentations and Methods

Phase identification was performed by using X-ray diffraction (XRD) using (XRD, Rigaku D/maxB, DMX-2200) and the Fourier transform infrared spectra in the range of 500–4000 cm^{-1} using a PerkinElmer IR spectrometer. The chemical state was examined via X-ray photoelectron spectroscopy (XPS, Thermo scientific multi-lab 2000, Waltham, MA, USA). The surface morphology was studied using scanning electron microscopy (JSM-6510series) and energy dispersive X-Ray (JEOL service advanced technology) spectroscopy. The electrochemical properties were explored using electrochemical impedance spectroscopy (EIS) through Autolab. CHI workstation was functional to carry out the electrochemical measurements in the three-electrode cell. The glassy carbon electrode (GCE) (surface area = 0.071 cm^2), saturated Ag|AgCl, and Pt wire were active as working, reference, and counter electrodes, respectively.

2.6. Fabrication of Electrode

The bare GCE was polished with alumina slurries, continued by ultrasonic cleaning in DI water/ethanol mixture for a few minutes, and later rinsed with ample DI water. To prepare electrocatalyst ink, 4 mg of ZnO HPs/P-CN composite was dispersed in 1 mL DI water with the assistance of ultrasonication for about 30 min at room temperature. Then, 5 μL of ZnO HPs/P-CN ink was coated onto a GCE surface, and then dried at a certain temperature. A similar protocol was followed to fabricate ZnO HPs-, P-CN- and g-CN-modified GCEs for electrochemical comparison study.

3. Results and Discussion

3.1. Physical Characterization of ZnO HPs/P-CN Composite

The crystallographic structure of the ZnO HPs/P-CN composite was obtained by an XRD technique (Figure 1A). The XRD patterns demonstrated that all diffraction peaks of the prepared sample are well-indexed with the standard spectrum diffraction peaks corresponding to the (100), (002), (101), (102), (110), (103), (200), (112), (201), (004), and (202) planes of ZnO (JCPDS no. 36–1451). The characteristic peaks located at 27.4° can be well-ascribed to the (002) planes of pure g-CN. Likewise, pronounced peaks at 27.4° were observed for P-CN [56]. The evident attenuation of the (002) peak intensity of P-CN reflected the heteroatom (P) substituted on the tri-s-triazine unit structure of CN nanosheets [53]. Hence, the intensity reduced while P-atoms were incorporated. It was mainly initiated by reducing the volume of piled carbon nitride interlayers and minor planar size of the constant tri-s-triazine unit disordered by P atoms [57]. The result obtained diffraction peaks corresponding to the (002), (100), (002), (101), (102), (110), (103), (200), (112), (201), (004), and (202) planes of the ZnO HPs/P-CN composite. It confirmed the formation of the ZnO HPs/P-CN composite.

Figure 1B represents the FTIR spectra, which characterized the functional groups and surface information of ZnO, g-CN, P-CN, and the ZnO HPs/P-CN composite. The foremost vibrational frequency (M-O) in ZnO was at 886 cm^{-1} owing to the Zn–O lattice [58]. P-CN kept similar vibration modes to g-CN, thus signifying that the P-doped 3D wrinkles structure array did not terminate the essential chemical structure of g-CN. The characteristic g-CN heterocycles in P-CN had stretching modes between 900 and 1700 cm^{-1} [59]. The peak M-O in the ZnO HPs/P-CN composite at 886 cm^{-1} was vibrational frequency owing to the Zn–O lattice and P-CN displayed peaks around between 900 and 1700 cm^{-1} in the ZnO HPs/P-CN composite.

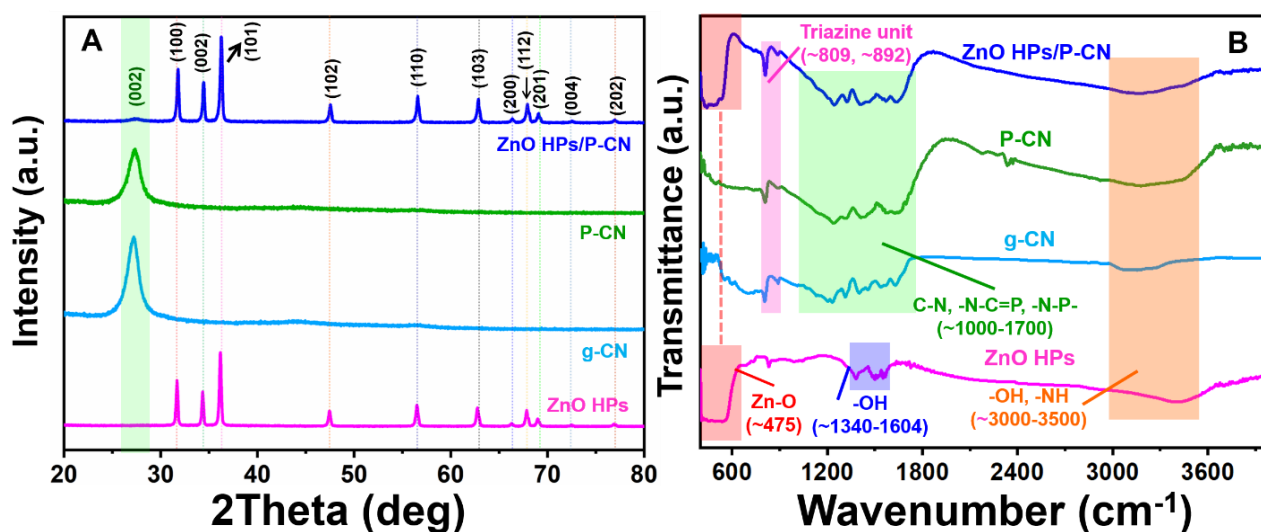


Figure 1. (A) XRD patterns and (B) FTIR spectra of ZnO HPs, g-CN, P-CN, and ZnO HPs/P-CN.

The XPS survey spectrum of the ZnO HPs/P-CN composite is shown in Figure 2A, where the peaks of Zn 2p, O 1s, C 1s, N 1s, and P 2p can be observed. Figure 2B represents a broad extended peak for Zn 2p_{3/2} and Zn 2p_{1/2} at a spectrum range of 1024.8 eV and 1047.9 eV, illustrating the presence of Zn lattice deities. Figure 2C shows that the O 1s spectrum attained at 533.9 eV could be ascribed to lattice oxygen as peaks of Zn–O bond. However, the weaker peak at 534.9 eV was related to oxygen in –OH species on the surface of ZnO. In the C 1s XPS spectrum (Figure 2D), the strong peak at a binding energy of 287.4 eV can be ascribed to carbon and the formation of defect-containing sp²-hybridized carbon atoms. The C 1s spectrum can be fitted with three peaks: C=O (288.8 eV), (N₂)–C=N (287.3 eV), and C–P–C (298.5 eV). Where the N 1s spectrum peak (Figure 2E) is a mixture of three adjacent peaks in which the strong peak attained at 399.6 eV is due to the Sp² hybridization of the triazine rings of N–(C) and the other two peaks are due to tertiary nitrogen radical deities and surface amino groups such as N–C=N and C=N–C compositions [60]. Where the doping of heteroatom sourced phosphorous P 2p signal (Figure 2F) is ascribed at a peak potential of 134.7 eV, which is an enclosure of two adjutant peaks attributed to the variation in P–N species of P 2p_{3/2} and P 2p_{1/2}, this variation in chemical composition indicates that the C atoms were replaced by P forming a P–N bonding, illustrating the P-CN structure [60–62].

SEM was adopted in observing the microscopic morphologies of the ZnO HPs/P-CN composite, as presented in Figure 3. As shown in Figure 3A, the ZnO material displays a hexagonal prism-like morphology with a smooth surface, with the inset image showing the hexagonal prism model. The pure g-CN (Figure 3B) was made of a nanosheets-like structure with wrinkles and stacking at the surface. It was observed that the P-CN (Figure 3C) possessed a 3D wrinkle-like morphology. The SEM of Figure 3D–F reveals the P-CN was well-dispersed on the ZnO HPs without agglomeration. This morphology would accelerate the transfer of electron rate and improve electrochemical properties. The elemental mapping images (Figure 4A–F) further confirmed the presence and homogeneous distributions of Zn, O, P, C, and N elements in the ZnO HPs/P-CN composite. The above physical characterization results were evident for the justification of ZnO HPs/P-CN composite formation.

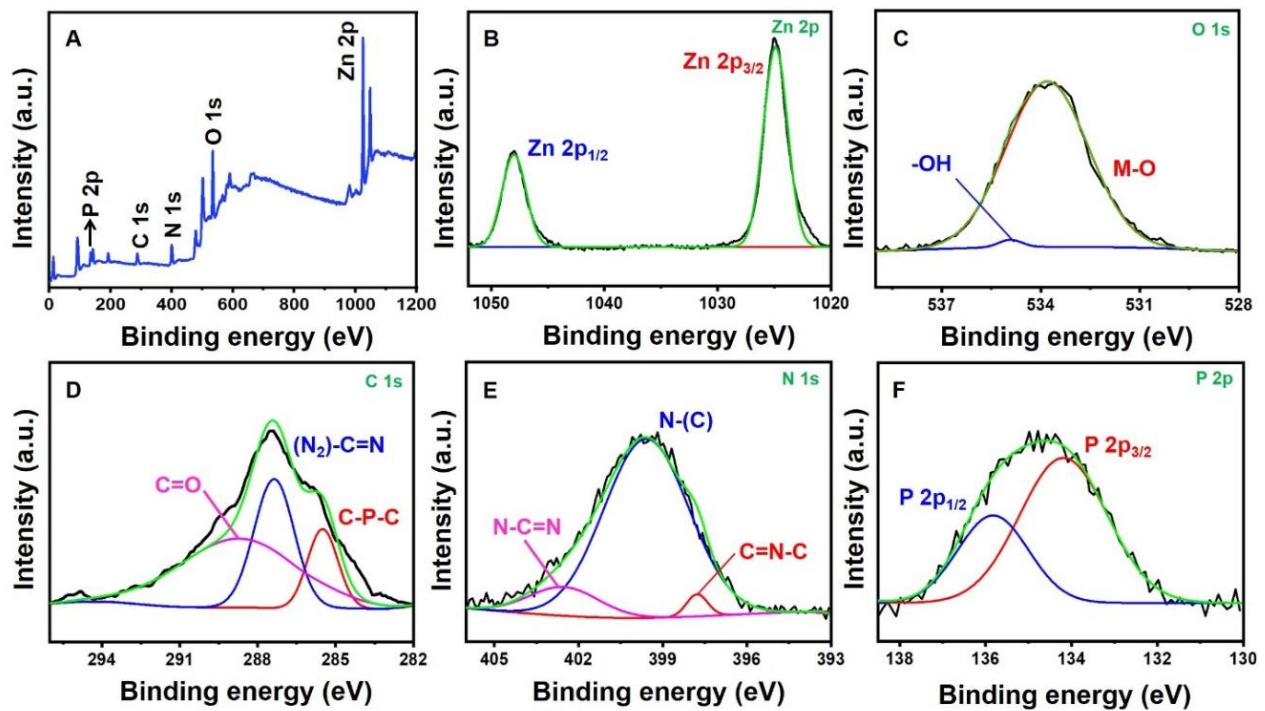


Figure 2. (A) A wide XPS survey spectra and fitting curves of high-resolution (B) Zn 2p, (C) O 1s, (D) C 1s, (E) N 1s, (F) P 2p of ZnO HPs/P-CN composite.

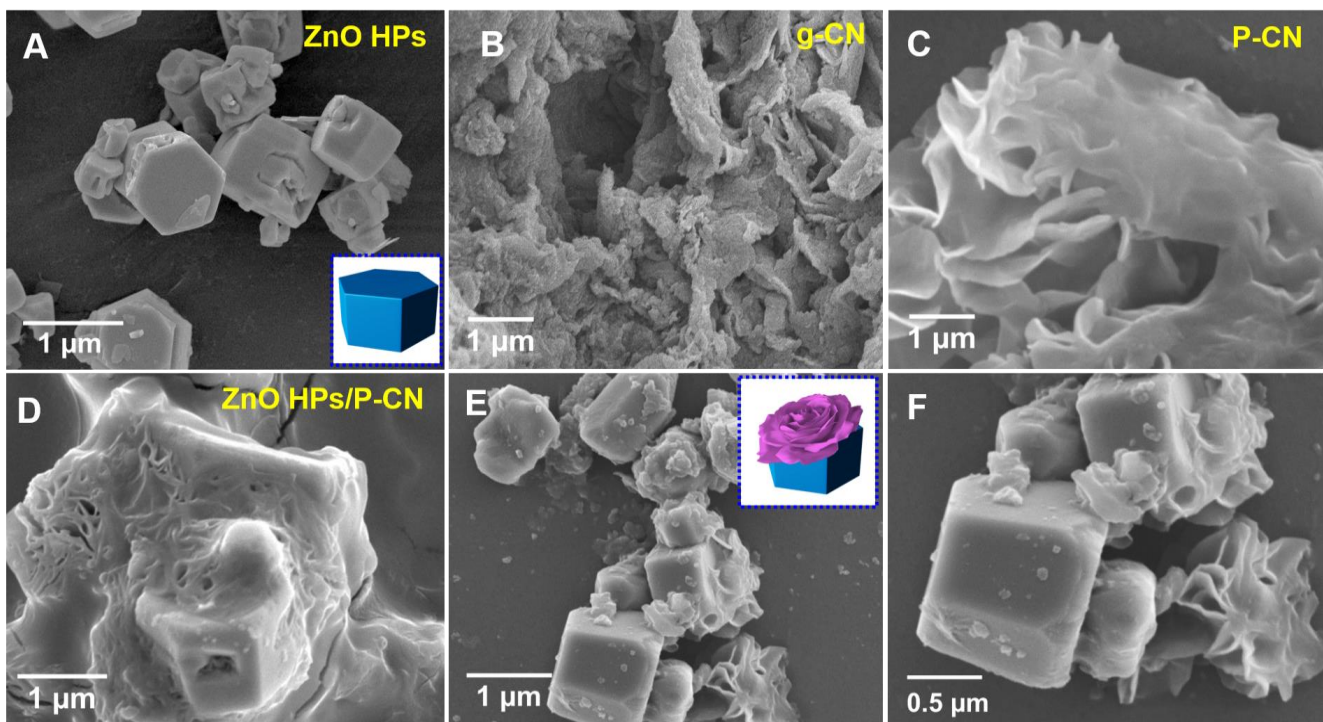


Figure 3. SEM images of (A) ZnO HPs (inset: hexagonal prism), (B) g-CN, (C) P-CN, and (D–F) ZnO HPs/P-CN composite (inset: wrinkle-like P-CN decorated on hexagonal prism).

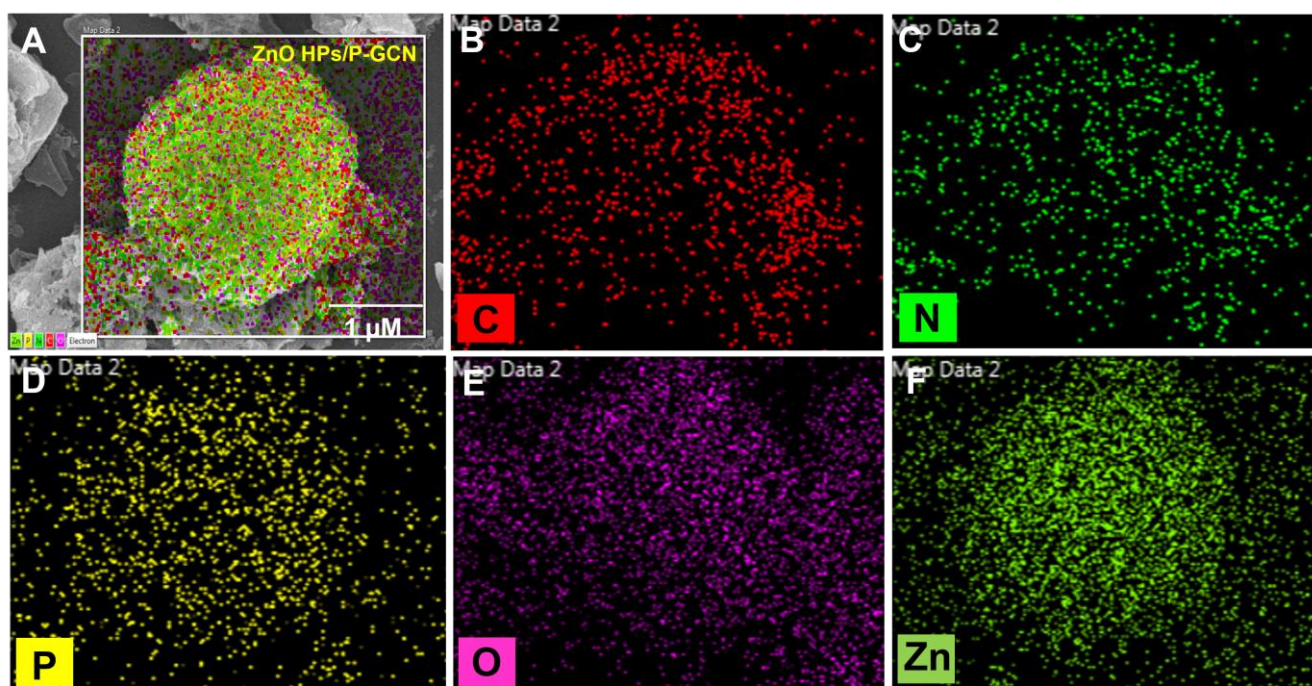


Figure 4. (A–F) Elemental mapping of ZnO HPs/P-CN composite.

3.2. Electrochemical Performance of ZnO HPs/P-CN Composite

3.2.1. Electrochemical Characterization

Electrochemical impedance spectroscopy (EIS) was employed to expose essential resistivity and concourse changes among modified and unmodified electrodes. Figure 5A demonstrates EIS curves derived for bare GCE, g-CN/GCE, P-CN/GCE, ZnO HPs/GCE, ZnO HPs/g-CN/GCE, and ZnO HPs/P-CN/GCE in 0.1 M KCl consisting of 5 mM $\text{Fe}(\text{CN})_6^{3-/4-}$. The Randles equivalent circuit model was utilized for investigating the electron charge transfer (R_{ct}), assembly of series resistance (R_s), double layer capacitance (C_{dl}), and Warburg diffusion (Z_w) which was attained to suit the experimental data and perform analysis, as shown in Figure 5A. As per the results, the bare GCE (1682.9 Ω) showed a larger R_{ct} value associated with the modified electrodes. Now, the R_{ct} value of the ZnO HPs/P-CN/GCE (102.2 Ω)-modified electrode seemed to be a smaller semicircle than the g-CN/GCE (1261.6 Ω), P-CN/GCE (884.8 Ω), ZnO HPs/GCE (677.8 Ω), and ZnO HPs/g-CN/GCE (253.4 Ω), which shows that owing to a smaller contact, less charge transfer impedance has happened in the modified electrodes. From the analysis results, the fabricated ZnO HPs/P-CN/GCE has an efficient electrochemical activity towards the determination of NF [63].

3.2.2. Electrochemical Behavior of Electrodes

The electrochemical behavior of the modified electrode with and without the addition of NF in 0.05 M PB (pH 7.0) was investigated by CV at the scan rate of 50 mV/s. This can be seen in Figure 5B, where a reduction peak of NF was observed at bare GCE, ZnO HPs/GCE, g-CN/GCE, P-CN/GCE, and ZnO HPs/P-CN/GCE, which is due to the direct electrocatalytic reduction of NF to phenyl hydroxylamine with the $4e^-/4H^+$ transfer process. During this reverse scan, there was not any anodic peak observed related to the reduction peak of NF, indicating that the catalytic reduction of NF is an irreversible process [64]. Among these electrodes, the ZnO HPs/P-CN/GCE showed a sharp and well-distinct reduction response of $-45.07 \mu\text{A}$ at about -0.35 V . The reduction response of NF at the ZnO HPs/P-CN/GCE is relatively 8.82-, 4.95-, 3.17-, 1.9-, and 1.62-folds greater than those of bare GCE, g-CN/GCE, P-CN/GCE, and ZnO HPs/GCE, respectively (Figure 5C). The preference of the electrochemical performance of the ZnO HPs/P-CN/GCE

compared to the other electrodes was credited to numerous advantages. Especially, the enhanced activity may be owed to the synergistic effect between ZnO HPs and P-CN in the composite towards NF reduction. Likewise, the ZnO HPs/P-CN composite provides a more active site, a large specific surface area, improved electrical conductivity, and favorable transportation. The proposed electrochemical mechanism of the ZnO HPs/P-CN modified electrode to NF was stated based on the literature (Scheme 2) [21–23]. The results proved that the best and good electrocatalytic properties were observed with the ZnO HPs/P-CN modified electrode.

3.2.3. Effects of Concentration, pH, and Scan Rate

The electrochemical performance of ZnO HPs/P-CN/GCE was evaluated by the CV approach with various concentrations of NF in 0.05M PB (pH 7.0) at a scan rate of 50 mV/s (Figure 5D). The electrochemical reduction current increased linearly with increasing target analyte concentrations ranging from 50 to 250 μM . The linear regression equation was expressed as $I_{pc} (\mu\text{A}) = -0.1511 [\text{NF}] (\mu\text{M}) - 8.648$ with a correlation coefficient (R^2) of 0.99 (Figure 5D inset image). These results suggest that the proposed ZnO HPs/P-CN/GC shows an outstanding catalytic performance towards detecting NF.

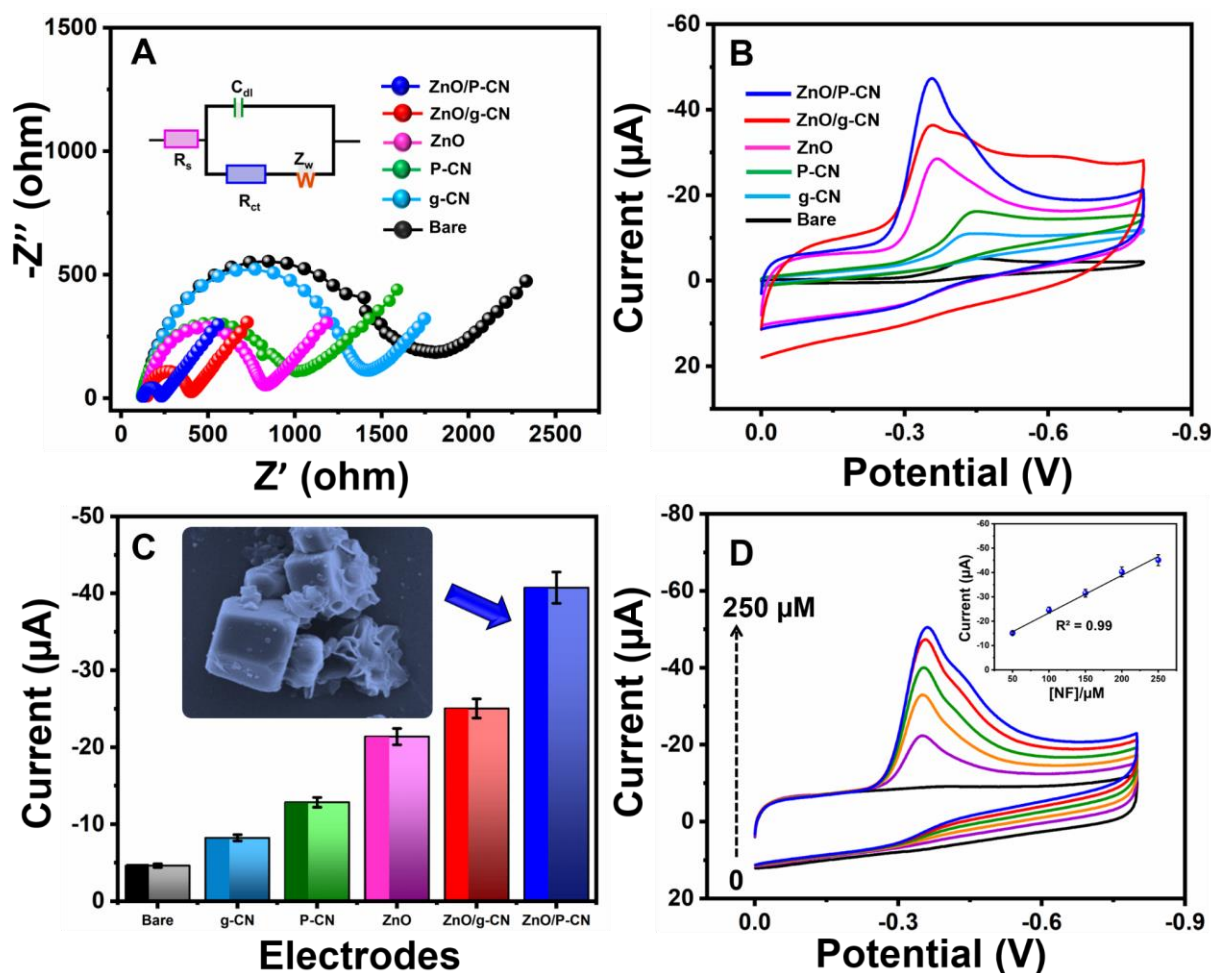
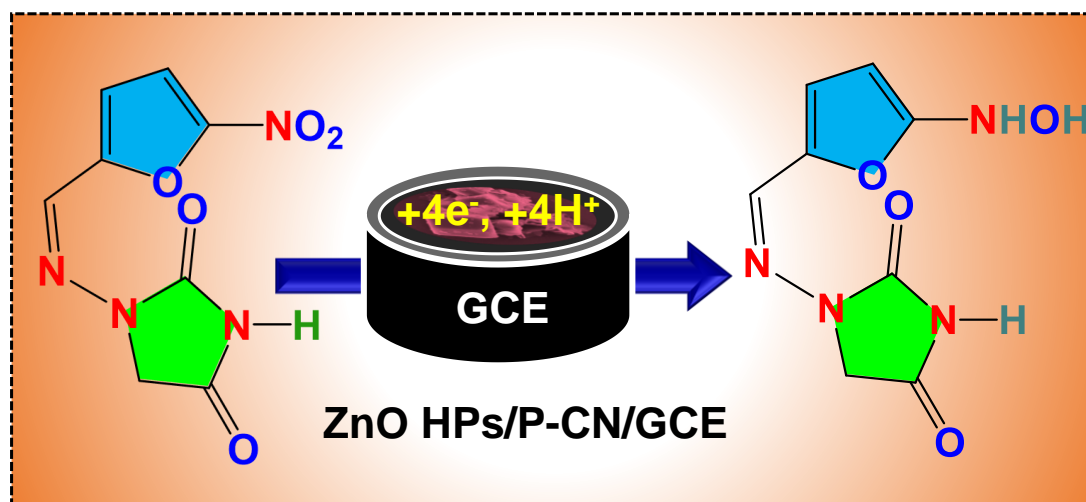


Figure 5. (A) EIS of bare GCE, g-CN/GCE, P-CN/GCE, ZnO HPs/GCE, ZnO HPs/g-CN/GCE, and ZnO HPs/P-CN/GCE (inset: Randles equivalent circuit). (B) CVs of unmodified and modified GCEs in 0.05 M PB presence of 200 μM NF. (C) Bar diagram for electrodes versus current from (B). (D) CVs of different concentrations of NF (50–250 μM) at ZnO HPs/P-CN/GCE in 0.05 M PB (inset: calibration plot of $[\text{NF}]/\mu\text{M}$ vs. current (μA)).



Scheme 2. The electrochemical reduction mechanism of NF.

The effect of the pH on the reduction response of NF was examined from pH 3.0 to 11.0 in 0.05 M PB using the ZnO HPs/P-CN/GCE (Figure 6A). As seen, the reduction current increased with increasing pH starting with 3.0 towards 7.0 and, beyond that, decreased when the pH was more than 7.0 for NF reduction, which is in agreement with the literature. We noted that the peak potential shifted for NF reduction towards more cathodic values with pH values increasing, which is due to the direct association of protons in the electrode reaction. In addition, a higher reduction current was observed at pH 7.0 (Figure 6B). Moreover, a linear relationship was observed between the reduction peak potential (E_{pc}) and pH values, as the following equation: $E_{pc} (\mu A) = y = -0.0385 \text{ pH} - 0.0865$ ($R^2 = 0.992$) (Figure 6B). A slope of 38.5 mV for each pH value was obtained, which is closer to the theoretical Nernstian value of 59 mV pH⁻¹, implying an electron transfer number conveyed by an equal quality of electrons and protons on the surface of ZnO HPs/P-CN/GCE. Hence, the 0.05M PB at pH 7.0 was chosen as the effective channel for subsequent NF electrochemical detection.

The influence of the scan rates on the electrochemical reduction response of NF at the ZnO HPs/P-CN-modified GCE was derived by the CV approach. Figure 6C displays the CV signals of ZnO HPs/P-CN/GCE in a 0.05 M PB (pH 7.0) containing 100 μM NF at different scan rates. The cathodic peaks current was amplified with the increasing scan rate in a range of 20–200 mV/s. A linear relationship between the reduction peak current and scan rate with a regression equation of $I_{pc} (\mu A) = -0.2605 v (\text{mV/s}) - 11.633$ ($R^2 = 0.995$) was observed (Figure 6D). The linear dependencies of the reduction peak currents on the sweep rate indicate that the ZnO HPs/P-CN-modified electrode is a process controlled by adsorption [65].

3.2.4. Electrochemical Detection of the Sensor

The quantitative analysis of NF on ZnO HPs/P-CN-modified GCE was carried out through the amperometry (i-t) method based on the optimal parameters. The reduction peak currents were found to be enhanced linearly with injection in the concentration of NF from 0.01 to 914 μM , as illustrated in Figure 7A. Our proposed electrochemical sensor detected NF with a linear region of concentration in 0.01–111 μM with a R^2 value of 0.997 (Figure 7B). The LOD and sensitivity were determined as 2 nM and 4.62 $\mu\text{A } \mu\text{M}^{-1} \cdot \text{cm}^2$ for the ZnO HPs/P-CN-modified electrode towards NF detection, respectively. The electrochemical performance of ZnO HPs/P-CN/GCE was compared with other previous NF sensors as shown in Table 1. These results demonstrate that the ZnO HPs/P-CN sensor exhibits greater electrochemical reduction ability towards NF sensing.

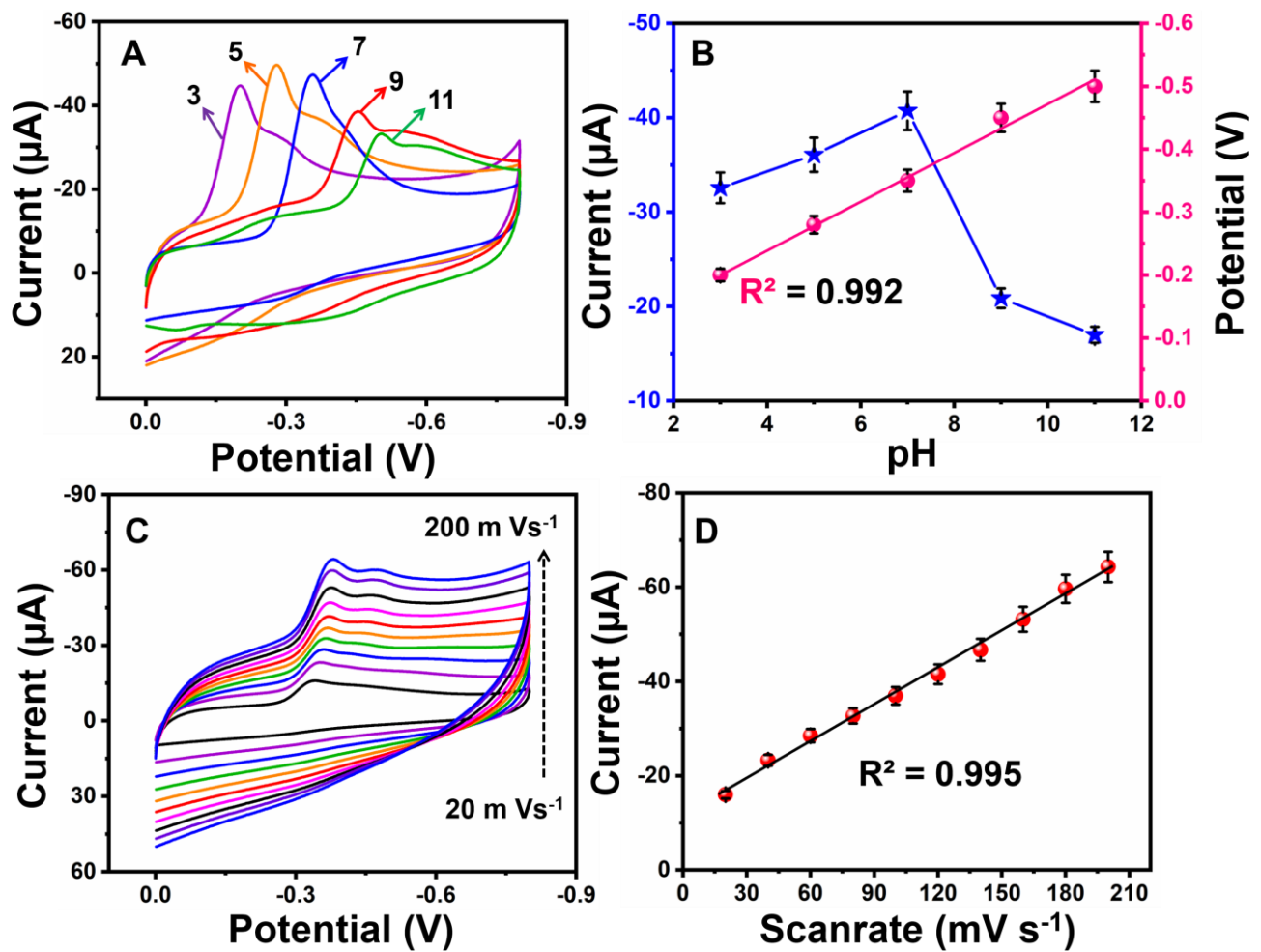


Figure 6. (A) CVs of ZnO HPs/P-CN/GCE in 0.05M PB with different pH containing 200 μM NF. (B) Effect of pH value on the I_{pc} and E_{pc} . (C) CVs of different scan rates (20–200 mV s^{-1}) of ZnO HPs/P-CN/GCE. (D) Corresponding linear plot of scan rates versus current.

Table 1. Analytical performance of the ZnO HPs/P-CN-modified electrode for NF determination compared with the previous literature.

Electrode Materials	Quantitative Method	Linear Range (μM)	Sensitivity ($\mu\text{A } \mu\text{M}^{-1} \text{cm}^{-2}$)	LOD (μM)	Ref.
ErGO-CNT	i-t	0.005–2.81	36.3	0.0187	[9]
LuV/GR	i-t	0.008–256	1.709	0.001	[10]
NiSnO	i-t	0.0066–466.6	–	0.003	[12]
rGO/Fe ₃ O ₄ NRs	DPV	0.1–100	–	0.083	[14]
NiO/BCN	i-t	0.05–230	1.15	0.01	[15]
BDDFE	SWV	0.497–5.66	–	0.0082	[21]
NiFe/f-MWCNT	DPV	0.1–352.4	11.45	0.03	[22]
MgFe ₂ O ₄	DPV	3–302	–	0.033	[23]
ZnO HPs/P-CN	i-t	0.01–111	4.62	0.002	This Work

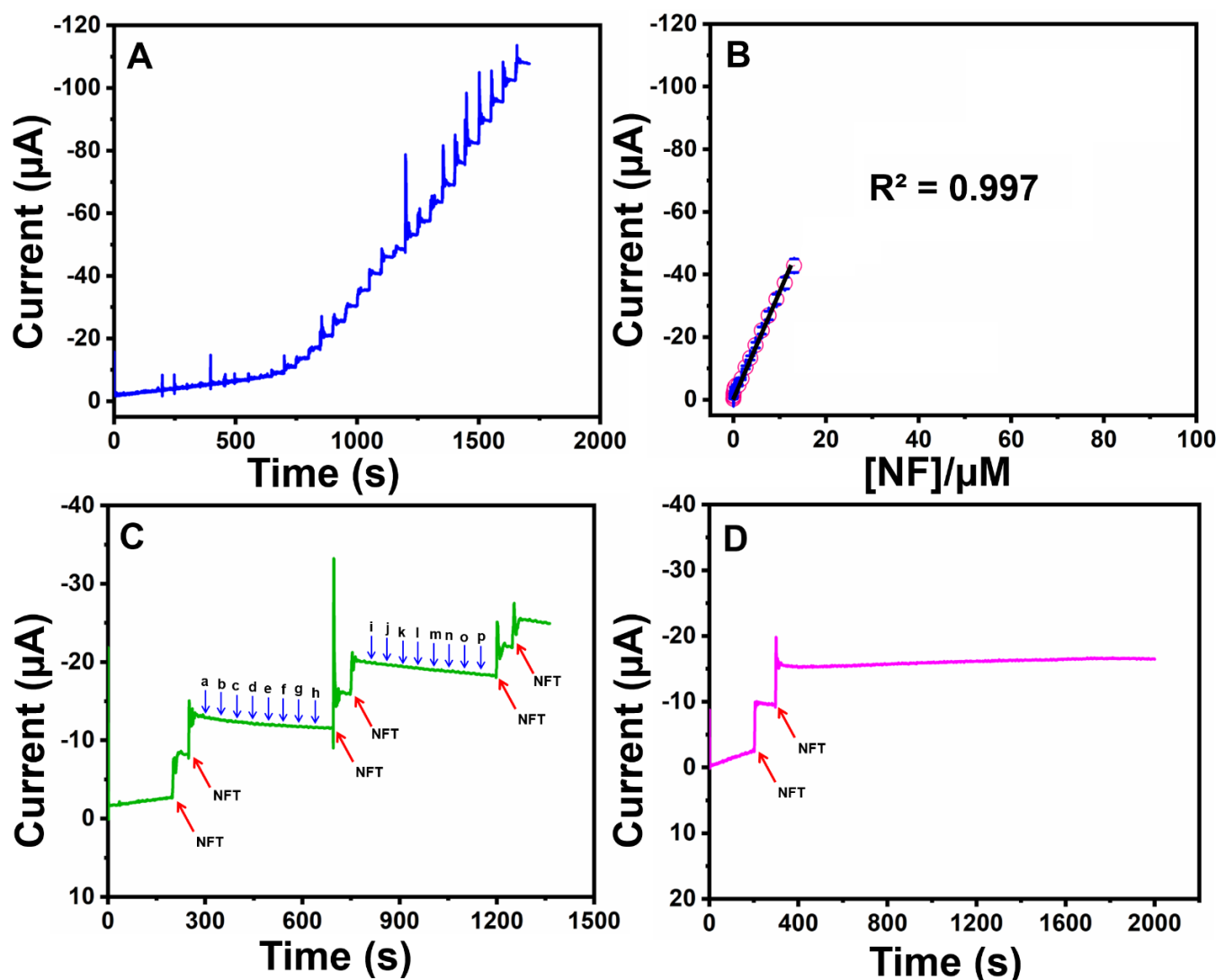


Figure 7. (A) The *i-t* responses of NF at the ZnO HPs/P-CN/GCE for the various additions of NF from 0.01 to 914 μM into constantly stirred 0.05 M PB (pH = 7.0). (B) Calibration plot of the concentration (NF/ μM) vs. current (μA). (C) Selectivity and (D) stability of the ZnO HPs/P-CN/GCE.

3.2.5. Specificity and Stability of the Sensor

The ZnO HPs/P-CN-modified electrode behavior toward NF sensing was inspected using the *i-t* technique in the occurrence of various potentially interfering species (Figure 7C). The anti-interference ability of the ZnO HPs/P-CN-modified electrode was examined towards NF with possible interferents, including furazolidone (a), nitrofurazone (b), 4-nitrophenol (c), chloramphenicol (d), flutamide (e), hydroquinone (f), catechol (g), uric acid (h), hydrogen peroxide (i), hypochlorous acid (j), sodium (k), nitrite (l), iron (m), mercury (n), copper (o), and lead (p). A 100-fold excess of a-g and 200-fold of h-p was added individually in the 0.05 M PB (pH 7.0) with 100 μM NF. There were almost no significant changes in NF response for potentially interfering species. The obtained results indicate that the ZnO HPs/P-CN-modified electrode has an outstanding selectivity towards NF sensing. The operational stability of the ZnO HPs/P-CN-modified electrode was evaluated with an injection of 100 μM NF (Figure 7D). The reduction current for NF maintains (\pm) 2.6% after 2000 s of the fabricated ZnO HPs/P-CN modified electrode. The above outcome reveals that the ZnO HPs/P-CN-modified electrode possesses superior selectivity and excellent stability.

3.2.6. Detection in Real Samples

The feasibility of the fabricated ZnO HPs/P-CN sensor was confirmed by its real-time analysis of NF in environmental and biological samples. The river water sample was used as the environmental and the urine samples were used as biological samples for detection of NF via the *i-t* technique. However, NF was not detected in the environmental and biological samples. To assess the practicability of the ZnO HPs/P-CN sensor, a standard solution with a known concentration of NF was spiked into the environmental and biological samples. The recovery rate of NF was estimated by a typical addition procedure. As displayed in Figure 8A,B, reduction peak current intensity increased step-wise with the addition of NF-spiked water, and the biological samples were in the range from 0.083 to 6 μM with a rapid response of 3 s. Based on the above, the fabricated ZnO HPs/P-CN sensor can accurately, and satisfactorily detect the NF in water and biological samples, which has confident application prospects in real-time applications.

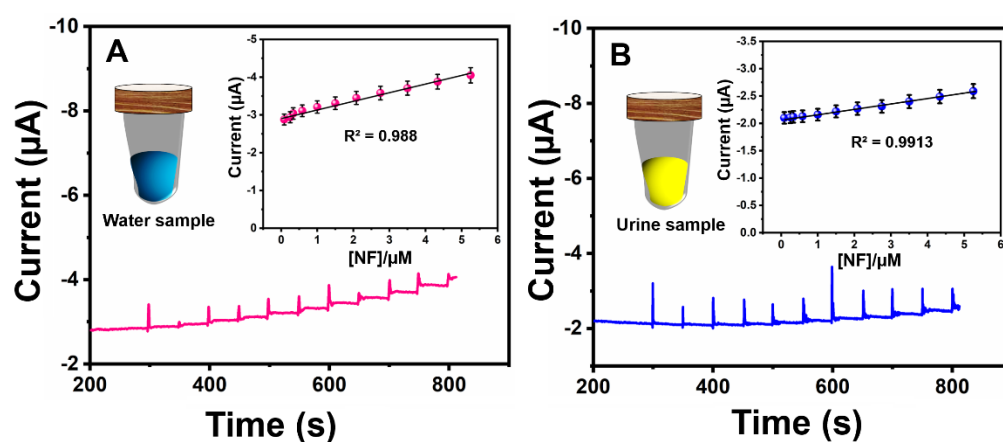


Figure 8. The amperometric real-world sample analysis responses in (A) water and (B) human urine samples of ZnO HPs/P-CN/GCE for the various additions of NF into constantly stirred 0.05 M PB (pH = 7.0).

4. Conclusions

In brief, we have effectively synthesized a ZnO HPs/P-CN composite for selective electrochemical detection of NF. The formation of the ZnO HPs/P-CN composite was confirmed by including XRD, FTIR, SEM, and elemental mapping. The ZnO HPs/P-CN composite modified electrode showed lower R_{ct} values than other modified electrodes with significant performance to the reduction of NF compared to the other electrodes. Particularly, the ZnO HPs/P-CN composite modified electrode displayed an advantage in its outstanding low detection limit, wide linear range, good sensitivity, high stability, and good selectivity. More importantly, the ZnO HPs/P-CN-based sensor was successful in detecting NF in environmental and human samples with high accuracy.

Author Contributions: Conceptualization, F.A., T.K. and A.U.; methodology F.A., T.K. and A.U.; validation, A.U., S.A. and N.M.S.; formal analysis, A.U., S.A., S.K. and N.A.; investigation, T.K.; resources, A.A. (Abdullah Aljaafari), A.A. (Adil Alshoaibi); data curation, F.A. and T.K.; writing—original draft preparation, F.A., T.K. and A.U.; writing—review and editing, F.A., T.K., A.U., S.A., M.G.A., A.A. (Abdullah Aljaafari) and A.A. (Adil Alshoaibi); visualization, N.A. and A.U.; supervision, F.A., T.K., A.U. and S.A.; project administration, F.A.; funding acquisition, F.A. All authors have read and agreed to the published version of the manuscript.

Funding: This work was supported by the Deanship of Scientific Research, Vice Presidency for Graduate Studies and Scientific Research, King Faisal University, Saudi Arabia [Project No. GRANT692] and the APC was funded by [Project No. GRANT692].

Institutional Review Board Statement: Not applicable.

Informed Consent Statement: Not applicable.

Data Availability Statement: Available on request.

Acknowledgments: This work was supported by the Deanship of Scientific Research, Vice Presidency for Graduate Studies and Scientific Research, King Faisal University, Saudi Arabia [Project No. GRANT692].

Conflicts of Interest: The authors declare no conflict of interest.

References

1. Chen, J.; Yang, W. Analysis of Nano-Silicon Dioxide Modified Waste Building Brick Materials in the Application of Adsorption and Removal of Water Pollutants. *Sci. Adv. Mater.* **2021**, *13*, 2393–2402. [[CrossRef](#)]
2. Qin, Y.; Li, W.; Akpınar, I.; Hang, C.; Huang, L.; Wang, L.; Gu, W.; Wu, J. Zeolitic Imidazolate Framework-8 (ZIF-8) and Its Derivative Nanomaterials for Antibiotics Adsorption in Contaminated Water. *J. Nanoelectron. Optoelectron.* **2021**, *16*, 1851–1860. [[CrossRef](#)]
3. Tan, X.; Zheng, Z.; Peng, B.; Wu, X.; Huang, X.; Chen, X. Simultaneous Degradation of p-Nitrophenol and Recovery of Copper from Wastewater in Electrochemical Reactor Under High Salinity. *Sci. Adv. Mater.* **2021**, *13*, 2450–2459. [[CrossRef](#)]
4. Gai, S.; Zhang, J.; Fan, R.; Xing, K.; Chen, W.; Zhu, K.; Zheng, X.; Wang, P.; Fang, X.; Yang, Y. Highly stable zinc-based metal-organic frameworks and corresponding flexible composites for removal and detection of antibiotics in water. *ACS Appl. Mater. Interfaces* **2020**, *12*, 8650–8662. [[CrossRef](#)]
5. Lu, F.; Astruc, D. Nanocatalysts and other nanomaterials for water remediation from organic pollutants. *Coord. Chem. Rev.* **2020**, *408*, 213180. [[CrossRef](#)]
6. Chen, H.; Xu, L.; Ai, W.; Lin, B.; Feng, Q.; Cai, K. Kernel functions embedded in support vector machine learning models for rapid water pollution assessment via near-infrared spectroscopy. *Sci. Total Environ.* **2020**, *714*, 136765. [[CrossRef](#)]
7. Li, X.-L.; Liang, Y.-L.; Li, M.-X.; Xin, L. Development of a Polyaluminum Ferric Titanium Chloride for Phosphorous Removal in Water. *Sci. Adv. Mater.* **2021**, *13*, 2287–2294. [[CrossRef](#)]
8. Yan, J.; Wei, Y.; Wen, Y.; Cai, H.; Xiao, J.; Wu, S.; Jin, S. Adsorption and Migration Characteristics of Fluorine in Ash-Sludging Water in Soils. *Sci. Adv. Mater.* **2021**, *13*, 705–717. [[CrossRef](#)]
9. Guo, R.; Liu, H.; Yang, K.; Wang, S.; Sun, P.; Gao, H.; Wang, B.; Chen, F. β -cyclodextrin polymerized in cross-flowing channels of biomass sawdust for rapid and highly efficient pharmaceutical pollutants removal from water. *ACS Appl. Mater. Interfaces* **2020**, *12*, 32817–32826. [[CrossRef](#)]
10. Jin, C.; Li, W.; Chen, Y.; Li, R.; Huo, J.; He, Q.; Wang, Y. Efficient photocatalytic degradation and adsorption of tetracycline over type-II heterojunctions consisting of ZnO nanorods and k-doped exfoliated g-c3n4 nanosheets. *Ind. Eng. Chem. Res.* **2020**, *59*, 2860–2873. [[CrossRef](#)]
11. Cook, S.M.; Vanduin, B.J.; Love, N.G.; Skerlos, S.J. Life cycle comparison of environmental emissions from three disposal options for unused pharmaceuticals. *Environ. Sci. Technol.* **2012**, *46*, 5535–5541. [[CrossRef](#)] [[PubMed](#)]
12. Khameneh, B.; Diab, R.; Ghazvini, K.; Bazzaz, B.S.F. Breakthroughs in bacterial resistance mechanisms and the potential ways to combat them. *Microb. Pathog.* **2016**, *95*, 32–42. [[CrossRef](#)]
13. Shokoohi, R.; Ghobadi, N.; Godini, K.; Hadi, M.; Atashzaban, Z. Antibiotic detection in a hospital wastewater and comparison of their removal rate by activated sludge and earthworm-based vermifiltration: Environmental risk assessment. *Process Saf. Environ. Prot.* **2020**, *134*, 169–177. [[CrossRef](#)]
14. Wang, Y.; Gong, C.; Zhu, Y.; Wang, Q.; Geng, L. Signal-on electrochemical aptasensor for sensitive detection of sulfamethazine based on carbon quantum dots/tungsten disulfide nanocomposites. *Electrochim. Acta* **2021**, *393*, 139054. [[CrossRef](#)]
15. Zarei, K.; Ghorbani, M. Fabrication of a new ultrasensitive AuNPs-MIC-based sensor for electrochemical determination of streptomycin. *Electrochim. Acta* **2019**, *299*, 330–338. [[CrossRef](#)]
16. Chelliah, K.; Vinothkumar, V.; Chen, S.M.; Sangili, A. Highly sensitive electrode materials for voltammetric determination of nitrofurantoin based zinc cobaltate nanosheet. *New J. Chem.* **2020**, *44*, 12036–12047. [[CrossRef](#)]
17. He, B.; Li, J. A sensitive electrochemical sensor based on reduced graphene oxide/Fe₃O₄ nanorod composites for detection of nitrofurantoin and its metabolite. *Anal. Methods* **2019**, *11*, 1427–1435. [[CrossRef](#)]
18. Wu, Y.; Liu, Y.; Tang, X.; Cheng, Z.; Liu, H. Tunable plasmonics of hollow raspberry-like nanogold for robust Raman scattering detection of antibiotic on portable Raman spectrometer. *Analyst* **2020**, *145*, 5854–5860. [[CrossRef](#)]
19. Sriram, B.; Baby, J.N.; Hsu, Y.F.; Wang, S.F.; George, M.; Veerakumar, P.; Lin, K.C. Electrochemical sensor-based barium zirconate on sulphur-doped graphitic carbon nitride for the simultaneous determination of nitrofurantoin (antibacterial agent) and nilutamide (anticancer drug). *J. Electroanal. Chem.* **2021**, *901*, 115782. [[CrossRef](#)]
20. Kummari, S.; Kumar, V.S.; Gobi, K.V. Facile Electrochemically reduced graphene oxide-multi-walled carbon nanotube nanocomposite as sensitive probe for in-vitro determination of nitrofurantoin in biological fluids. *Electroanalysis* **2020**, *32*, 2452–2462. [[CrossRef](#)]
21. Kokulnathan, T.; Chen, S.M. Robust and selective electrochemical detection of antibiotic residues: The case of integrated lutetium vanadate/graphene sheets architectures. *J. Hazard. Mater.* **2019**, *384*, 121304. [[CrossRef](#)] [[PubMed](#)]

22. Kokulnathan, T.; Wang, T.J. Synthesis and characterization of 3D flower-like nickel oxide entrapped on boron doped carbon nitride nanocomposite: An efficient catalyst for the electrochemical detection of nitrofurantoin. *Compos. Part B Eng.* **2019**, *174*, 106914. [[CrossRef](#)]
23. Annalakshmi, M.; Sumithra, S.; Chen, S.M.; Chen, T.W.; Zheng, X.H. Facile synthesis of ultrathin NiSnO₃ nanoparticles for enhanced electrochemical detection of an antibiotic drug in water bodies and biological samples. *New J. Chem.* **2020**, *44*, 10604–10612. [[CrossRef](#)]
24. Alrassol, K.S.A.; Qasim, Q.A.; Ahmed, G.S.; Al-Salman, H.N.K. A modified and credible methods to estimate nitrofurantoin in the standard of substances and pharmaceutical dosage. *Int. J. Pharm. Res.* **2019**, *11*, 1057–1072. [[CrossRef](#)]
25. Huo, J.C.; Yang, H.X.; Ma, Y.; Bai, J. Lightweight, Flexible and Hydrophobic Cotton Fiber/Silica Aerogel Composite by Freeze-Drying for Organic Solvent/Water Separation and Thermal Insulation. *Sci. Adv. Mater.* **2021**, *13*, 1820–1824. [[CrossRef](#)]
26. Huttner, E.; Verhaegh, M.; Harbarth, S.; Muller, A.E.; Theuretzbacher, U.; Mouton, J.W. Nitrofurantoin revisited: A systematic review and meta-analysis of controlled trials. *J. Antimicrob. Chemother.* **2015**, *70*, 2456–2464. [[CrossRef](#)]
27. Hang, C.; Akpinar, I.; Qin, Y.; Huang, L.; Wang, L.; Li, W.; Wu, J. A Review on Adsorption of Organic Pollutants from Water by UiO-67 and Its Derivatives. *J. Nanoelectron. Optoelectron.* **2021**, *16*, 1861–1873. [[CrossRef](#)]
28. Wang, Y.; Chen, T.; Zhuang, Q.; Ni, Y. Label-free photoluminescence assay for nitrofurantoin detection in lake water samples using adenosine-stabilized copper nanoclusters as nanoprobes. *Talanta* **2018**, *179*, 409–413. [[CrossRef](#)]
29. Meng, M.; Qin, N.; Sun, L.; Chen, Y.; Xu, K.; Zhang, Y.; Liu, M.; Du, S.; Liu, K.; Feng, Y.; et al. Lightweight 3D-TiO₂ Nanotube Arrays on Ti Mesh for Promoted Photoelectrochemical Water Splitting. *J. Nanoelectron. Optoelectron.* **2021**, *16*, 1342–1347. [[CrossRef](#)]
30. Harrison, J.; Lewis, D.A.; Ancill, R.J. The spectrophotometric determination of nitrofurantoin in blood and urine. *Analyst* **1973**, *98*, 146. [[CrossRef](#)] [[PubMed](#)]
31. Mazzara, F.; Patella, B.; Aiello, G.; O’Riordan, A.; Torino, C.; Vilasi, A.; Inguanta, R. Electrochemical detection of uric acid and ascorbic acid using r-GO/NPs based sensors. *Electrochim. Acta* **2021**, *388*, 138652. [[CrossRef](#)]
32. Kokulnathan, T.; Wang, T.-J.; Kumar, E.A.; Ahmed, F. Construction of nickel cobalt-layered double hydroxide/functionalized-halloysite nanotubes composite for electrochemical detection of organophosphate insecticide. *Chem. Eng. J.* **2021**, *433*, 133639. [[CrossRef](#)]
33. Joseph, X.B.; Baby, J.N.; Wang, S.-F.; Sriram, B.; George, M. Interfacial superassembly of Mo₂C@NiMn-LDH frameworks for electrochemical monitoring of carbendazim fungicide. *ACS Sustain. Chem. Eng.* **2021**, *9*, 14900–14910. [[CrossRef](#)]
34. Sriram, B.; Baby, J.N.; Wang, S.F.; Hsu, Y.F.; Sherlin, V.A.; George, M. Well-designed construction of yttrium orthovanadate confined on graphitic carbon nitride sheets: Electrochemical investigation of dimetridazole. *Inorg. Chem.* **2021**, *60*, 13150–13160. [[CrossRef](#)] [[PubMed](#)]
35. Muthukutty, B.; Ganesamurthi, J.; Chen, S.M.; Arumugam, B.; Maochang, F.; Wabaidur, S.M.; Othman, Z.A.A.L.; Altalhi, T.; Ali, M.A. Construction of novel binary metal oxides: Copper oxide–tin oxide nanoparticles regulated for selective and nanomolar level electrochemical detection of anti-psychotic drug. *Electrochim. Acta* **2021**, *386*, 138482. [[CrossRef](#)]
36. Mehta, S.K.; Singh, K.; Umar, A.; Chaudhary, G.R.; Singh, S. Ultra-high sensitive hydrazine chemical sensor based on low-temperature grown ZnO nanoparticles. *Electrochim. Acta* **2012**, *69*, 128–133. [[CrossRef](#)]
37. Yang, T.; Chen, M.; Kong, Q.; Wang, X.; Guo, X.; Li, W.; Jiao, K. Shape-controllable ZnO nanostructures based on synchronously electrochemically reduced graphene oxide and their morphology-dependent electrochemical performance. *Electrochim. Acta* **2015**, *182*, 1037–1045. [[CrossRef](#)]
38. Dong, Q.; Ryu, H.; Lei, Y. Metal oxide based non-enzymatic electrochemical sensors for glucose detection. *Electrochim. Acta* **2021**, *370*, 137744. [[CrossRef](#)]
39. Hatamluyi, B.; Es’haghi, Z. Electrochemical biosensing platform based on molecularly imprinted polymer reinforced by ZnO-graphene capped quantum dots for 6-mercaptopurine detection. *Electrochim. Acta* **2018**, *283*, 1170–1177. [[CrossRef](#)]
40. Saritha, D.; Koirala, A.R.; Venu, M.; Reddy, G.D.; Reddy, A.V.B.; Sitaram, B.; Madhavi, G.; Aruna, K. A simple, highly sensitive and stable electrochemical sensor for the detection of quercetin in solution, onion and honey buckwheat using zinc oxide supported on carbon nanosheet (ZnO/CNS/MCPE) modified carbon paste electrode. *Electrochim. Acta* **2019**, *313*, 523–531. [[CrossRef](#)]
41. George, J.M.; Antony, A.; Mathew, B. Metal oxide nanoparticles in electrochemical sensing. *Microchim. Acta* **2018**, *185*, 358. [[CrossRef](#)]
42. Napi, M.L.M.; Sultan, S.M.; Ismail, R.; How, K.W.; Ahmad, M.K. Electrochemical-based biosensors on different zinc oxide nanostructures: A review. *Materials* **2019**, *12*, 2985. [[CrossRef](#)] [[PubMed](#)]
43. Kokulnathan, T.; Wang, T.-J. Vanadium carbide-entrapped graphitic carbon nitride nanocomposites: Synthesis and electrochemical platforms for accurate detection of furazolidone. *ACS Appl. Nano Mater.* **2020**, *3*, 2554–2561. [[CrossRef](#)]
44. Cao, Y.; Wang, L.; Wang, C.; Hu, X.; Liu, Y.; Wang, G. Sensitive detection of glyphosate based on a Cu-BTC MOF/g-C₃N₄ nanosheet photoelectrochemical sensor. *Electrochim. Acta* **2019**, *317*, 341–347. [[CrossRef](#)]
45. Ponnaiah, S.K.; Prakash, P.; Vellaichamy, B.; Paulmony, T.; Selvanathan, R. Picomolar-level electrochemical detection of thiocyanate in the saliva samples of smokers and non-smokers of tobacco using carbon dots doped Fe₃O₄ nanocomposite embedded on g-C₃N₄ nanosheets. *Electrochim. Acta* **2018**, *283*, 914–921. [[CrossRef](#)]
46. Kokulnathan, T.; Chen, S.M. Praseodymium vanadate-decorated sulfur-doped carbon nitride hybrid nanocomposite: The role of a synergistic electrocatalyst for the detection of metronidazole. *ACS Appl. Mater. Interfaces* **2019**, *11*, 7893–7905. [[CrossRef](#)]

47. Sriram, B.; Baby, J.N.; Wang, S.F.; Govindasamy, M.; George, M.; Jothiramalingam, R. Cobalt molybdate nanorods decorated on boron-doped graphitic carbon nitride sheets for electrochemical sensing of furazolidone. *Microchim. Acta* **2020**, *187*, 654. [[CrossRef](#)]
48. Li, J.; Qi, Y.; Mei, Y.; Ma, S.; Li, Q.; Xin, B.; Yao, T.; Wu, J. Construction of phosphorus-doped carbon nitride/phosphorus and sulfur co-doped carbon nitride isotype heterojunction and their enhanced photoactivity. *J. Colloid Interface Sci.* **2020**, *566*, 495–504. [[CrossRef](#)]
49. Su, J.; Geng, P.; Li, X.; Zhao, Q.; Quan, X.; Chen, G. Novel phosphorus doped carbon nitride modified TiO₂ nanotube arrays with improved photoelectrochemical performance. *Nanoscale* **2015**, *7*, 16282–16289. [[CrossRef](#)]
50. Li, B.; Si, Y.; Fang, Q.; Shi, Y.; Huang, W.Q.; Hu, W.; Pan, A.; Fan, X.; Huang, G.F. Hierarchical self-assembly of well-defined louver-like p-doped carbon nitride nanowire arrays with highly efficient hydrogen evolution. *Nano-Micro Lett.* **2020**, *12*. [[CrossRef](#)]
51. Kesavan, T.; Partheeban, T.; Vivekanantha, M.; Prabu, N.; Kundu, M.; Selvarajan, P.; Umopathy, S.; Vinu, A.; Sasidharan, M. Design of p-doped mesoporous carbon nitrides as high-performance anode materials for li-ion battery. *ACS Appl. Mater. Interfaces* **2020**, *12*, 24007–24018. [[CrossRef](#)]
52. Ren, J.T.; Wang, Y.S.; Chen, L.; Gao, L.J.; Tian, W.W.; Yuan, Z.Y. Binary FeNi phosphides dispersed on N, P-doped carbon nanosheets for highly efficient overall water splitting and rechargeable Zn-air batteries. *Chem. Eng. J.* **2020**, *389*, 124408. [[CrossRef](#)]
53. Liu, B.; Ye, L.; Wang, R.; Yang, J.; Zhang, Y.; Guan, R.; Tian, L.; Chen, X. Phosphorus-doped graphitic carbon nitride nanotubes with amino-rich surface for efficient CO₂ capture, enhanced photocatalytic activity, and Product Selectivity. *ACS Appl. Mater. Interfaces* **2018**, *10*, 4001–4009. [[CrossRef](#)]
54. Wang, X.; Wang, W.; Miao, Y.; Feng, G.; Zhang, R. Facet-selective photodeposition of gold nanoparticles on faceted ZnO crystals for visible light photocatalysis. *J. Colloid Interface Sci.* **2016**, *475*, 112–118. [[CrossRef](#)]
55. Hussain, S.K.; Yu, J.S. Cobalt-doped zinc manganese oxide porous nanocubes with controlled morphology as positive electrode for hybrid supercapacitors. *Chem. Eng. J.* **2019**, *361*, 1030–1042. [[CrossRef](#)]
56. Sriram, B.; Baby, J.N.; Hsu, Y.F.; Wang, S.F.; Joseph, X.B.; George, M.; Veerakumar, P.; Lin, K.C. MnCo₂O₄ microflowers anchored on P-doped g-C₃N₄ nanosheets as an electrocatalyst for voltammetric determination of the antibiotic drug sulfadiazine. *ACS Appl. Electron. Mater.* **2021**, *3*, 3915–3926. [[CrossRef](#)]
57. Ma, T.Y.; Dai, S.; Jaroniec, M.; Qiao, S.Z. Graphitic carbon nitride nanosheet–carbon nanotube three-dimensional porous composites as high-performance oxygen evolution electrocatalysts. *Angew. Chem.* **2014**, *126*, 7409–7413. [[CrossRef](#)]
58. Gutul, T.; Rusu, E.; Condur, N.; Ursaki, V.; Goncarenco, E.; Vlazan, P. Preparation of poly(N-vinylpyrrolidone)-stabilized zno colloid nanoparticles. *Beilstein J. Nanotechnol.* **2014**, *5*, 402–406. [[CrossRef](#)]
59. Qiu, Y.; Xin, L.; Jia, F.; Xie, J.; Li, W. Three-dimensional phosphorus-doped graphitic-C₃N₄ self-assembly with NH₂-functionalized carbon composite materials for enhanced oxygen reduction reaction. *Langmuir* **2016**, *32*, 12569–12578. [[CrossRef](#)]
60. Zhang, L.; Chen, X.; Guan, J.; Jiang, Y.; Hou, T.; Mu, X. Facile synthesis of phosphorus doped graphitic carbon nitride polymers with enhanced visible-light photocatalytic activity. *Mater. Res. Bull.* **2013**, *48*, 3485–3491. [[CrossRef](#)]
61. Guo, S.; Deng, Z.; Li, M.; Jiang, B.; Tian, C.; Pan, Q.; Fu, H. Phosphorus-doped carbon nitride tubes with a layered micro-nanostructure for enhanced visible-light photocatalytic hydrogen evolution. *Angew. Chem.* **2016**, *128*, 1862–1866. [[CrossRef](#)]
62. Zhao, S.; Liu, Y.; Wang, Y.; Fang, J.; Qi, Y.; Zhou, Y.; Bu, X.; Zhuo, S. Carbon and phosphorus co-doped carbon nitride hollow tube for improved photocatalytic hydrogen evolution. *J. Colloid Interface Sci.* **2022**, *616*, 152–162. [[CrossRef](#)] [[PubMed](#)]
63. deLima-Neto, P.; Correia, A.N.; Portela, R.R.; Julião, M.d.; Linhares-Junior, G.F.; deLima, J.E.S. Square wave voltammetric determination of nitrofurantoin in pharmaceutical formulations on highly boron-doped diamond electrodes at different boron-doping contents. *Talanta* **2010**, *80*, 1730–1736. [[CrossRef](#)] [[PubMed](#)]
64. Hwa, K.Y.; Sharma, T.S.K. Nano assembly of NiFe spheres anchored on f-MWCNT for electrocatalytic reduction and sensing of nitrofurantoin in biological samples. *Sci. Rep.* **2020**, *10*, 12256. [[CrossRef](#)] [[PubMed](#)]
65. Baby, J.N.; Sriram, B.; Wang, S.F.; George, M. Effect of various deep eutectic solvents on the sustainable synthesis of MgFe₂O₄ nanoparticles for simultaneous electrochemical determination of nitrofurantoin and 4-nitrophenol. *ACS Sustain. Chem. Eng.* **2020**, *8*, 1479–1486. [[CrossRef](#)]